crystals

MDPI

Article

Development of $Co(OH)_xF_{2-x}$ Nanosheets for Acetone Gas Sensor Applications: Material Characterization and Sensor Performance Evaluation

Yaping Yan [1,2,†], Tae-yil Eom [3,†], Shiyu Xu [4], Pil J. Yoo [4], Changzeng Yan [5], Joon-Shik Park [6,*] and Hoo-Jeong Lee [2,3,*,‡]

1 International Collaborative Laboratory of 2D Materials for Optoelectronics Science and Technology of Ministry of Education, Institute of Microscale Optoelectronics, Shenzhen University, Shenzhen 518060, China; yanyaping0512@163.com
2 School of Advanced Materials Science and Engineering, Sungkyunkwan University, Suwon 16419, Korea
3 SKKU Advanced Institute of Nano Technology, Sungkyunkwan University, Suwon 16419, Korea; ety1106@skku.edu
4 School of Chemical Engineering, Sungkyunkwan University, Suwon 16419, Korea; xushiyu@skku.edu (S.X.); pjyoo@skku.edu (P.J.Y.)
5 Shenzhen Institute of Advanced Electronic Materials—Shenzhen Institutes of Advanced Technology, Chinese Academy of Sciences, Shenzhen 518055, China; yanchangzeng@163.com
6 Smart Sensor Research Center, Korea Electronics Technology Institute (KETI), Seongnam 13509, Korea
* Correspondence: jspark@keti.re.kr (J.-S.P.); hlee@skku.edu (H.-J.L.)
† These 1st authors equally contributed to this work.
‡ Current address: Department of Smart Fab. Technology, Sungkyunkwan University, Suwon 16419, Korea.

Received: 9 October 2020; Accepted: 23 October 2020; Published: 26 October 2020

Abstract: This study reports the employment of $Co(OH)_xF_{2-x}$ nanosheets, a new material in the sensor field, for gas sensor applications. We synthesize $Co(OH)_xF_{2-x}$ nanosheets via a hydrothermal route using SiO_2 sphere templates. Our material characterization confirms that the material is a densely clustered $Co(OH)_xF_{2-x}$ nanosheet with an amorphous microstructure with some short-range ordering. Sensors based on the nanosheets demonstrate a high response of 269% toward 4.5 ppm of acetone gas at an operation temperature of 200 °C and a very low minimum detection limit of 40 ppb. It functions effectively up to a temperature below 300 °C, above which F is found to start to evaporate. Our discussion suggests that an excellent sensor performance arises from the high catalytic function of F incorporated in a high concentration in the material as well as the high specific surface area due to the morphology of densely clustered nanosheets.

Keywords: $Co(OH)_xF_{2-x}$; SiO_2 spheres template; nanosheets; acetone gas sensor; low-concentration detection

1. Introduction

There is a growing demand for the sensitive detection of acetone due to its possible usage as a breath marker for the diagnosis of diseases such as diabetes [1]. For breath marker applications, a very high sensitivity (sub-ppm level or lower) is necessary since the exhaled acetone concentration range is very low—from 0.3 to 1.8 ppm [2,3]. Due to the low cost and simplicity of fabrication/operation, metal oxide semiconductors, such as ZnO, SnO_2, and Co_3O_4, have been actively explored as acetone sensor materials [4–7]. Among them, Co_3O_4, as a p-type material, is a promising candidate for acetone sensor materials due to its low and stable initial resistance and the high catalytic reactivity of Co^{2+} [8–11]. In a study conducted by Vladimirova et al., for instance, the tolerance of Co_3O_4 toward high humidity levels is discussed [12]. In experiments by Zhang et al., a Co_3O_4-based sensor with an optimized morphology

of crossed nanosheets showed a response of 36.5 toward acetone gas of 1000 ppm. Zhang et al. also reported Co_3O_4 nanowires being hybridized with hollow carbon spheres exhibiting a response of 3.71 toward acetone gas of 200 ppm [13]. Xu et al. synthesized metal-organic framework (MOF)-derived Co_3O_4/Fe_2O_3 p-n hollow cubes to enhance acetone sensing properties (response of 3.27 to 100 ppm) [14]. However, the detection of acetone at a low concentration (sub-ppm or lower) still remains a challenge.

Doping metal oxide materials with fluorine, known to promote catalytic activity, has been considered as one of the effective routes to enhance sensing ability [15,16]. Barreca et al. employed $Co(hfa)_2$·TMEDA (hfa = 1,1,1,5,5,5-hexafluoro-2,4-pentanedionate; TMEDA = N,N,N′,N′-tetramethylethylenediamine) as a precursor in chemical vapor deposition to produce F-doped Co_3O_4 nanomaterials [15]. Nonetheless, such a doping method has a limitation in obtaining a fluorine concentration high enough for a significant sensitivity improvement. Recently, cobalt fluoride hydroxide ($Co(OH)_xF_{2-x}$), a material including F anions as one of its main elements, came into the spotlight for being applied to catalysts for water oxidation, hydrogen production, and overall water splitting, taking full advantage of the high catalytic activity of F anions in the materials [9,17–19]. Nevertheless, a challenge to employ this material for gas sensor applications is its poor thermal stability: it could easily transform into Co_3O_4 via fluorine evaporation during a high temperature process such as the aging process (200~450 °C) which is usually required for sensor fabrication [20].

In this study, we report, for the first time, $Co(OH)_xF_{2-x}$ nanosheets employed as a sensing material for acetone gas sensors. We synthesized $Co(OH)_xF_{2-x}$ nanosheets via a hydrothermal route on the template of SiO_2 spheres. Our synthesis method using the SiO_2 spheres as template helped achieve a high fluorine density and suppress fluorine evaporation to a considerable extent upon annealing at elevated temperatures. Sensors fabricated using the $Co(OH)_xF_{2-x}$ materials showcased a high response at a low acetone concentration (269% at 4.5 ppm) and ppb-level detection limit (~40 ppb) at an operation temperature of 200 °C. We also discussed the effects of F anions on the sensing properties of $Co(OH)_xF_{2-x}$ nanosheets.

2. Materials and Methods

2.1. Fabrication of $Co(OH)_xF_{2-x}$ Nanosheets

All the chemicals were used without any purification. Figure 1 shows the schematic diagram of the synthesis procedure used for the fabrication of $Co(OH)_xF_{2-x}$ nanosheets. SiO_2 spheres were synthesized using tetraethyl orthosilicate (TEOS) as described in another report [21]. $Co(OH)_xF_{2-x}$ nanosheets were synthesized as follows. $CoCl_2$ (0.3 mM), NH_4F (0.3 mM), and urea (0.1 mM) were added into de-ionized (DI) water (30 mL). After stirring for 30 min, the SiO_2 spheres (60 mg) were added into the solution, followed by sonication for 30 min. Finally, the solution was transferred to a Teflon-lined steel autoclave with a capacity of 50 mL and heated at 120 °C for 12 h under autogenous pressure. The final solution was then cooled to room temperature. Powder, precipitated from the solution, was collected by filtering and was washed with water and ethanol. The powder was then dried at 80 °C overnight. It went through a subsequent aging process at 120 °C for 10 h for removal of the SiO_2 sacrificial template [22]. Chemical analysis using electron dispersive spectroscopy (EDS; EDS attached to the JEOL ARM 200F), nevertheless, disclosed that some SiO_2 had remained in the sample after the removal process (see Supplementary Materials Figure S1). For comparison, some materials were synthesized without templates via the same process.

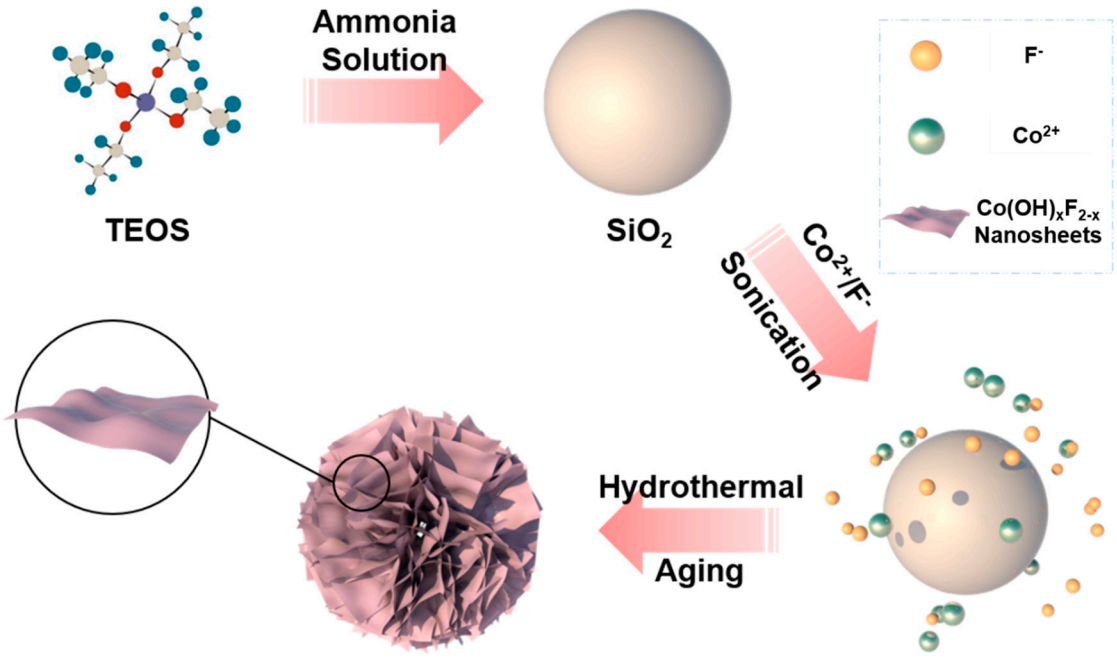

Figure 1. Illustration of the synthesis process of $Co(OH)_xF_{2-x}$ nanosheets.

2.2. Characterization

Scanning electron microscopy (SEM; JSM-7600F, JEOL, Tokyo, Japan) and transmission electron microscopy (TEM; JEM-ARM 200F, JEOL, Tokyo, Japan) were used to investigate the morphology of the SiO_2 spheres and $Co(OH)_xF_{2-x}$ nanosheets. The infrared spectra of materials were recorded using Fourier transform infrared spectroscopy (FTIR; IFS-66/S, Bruker, Billerica, MA, USA). For characterization of the phases of the materials, X-ray diffraction (XRD; D8 Advance diffractometer, Bruker, Billerica, MA, USA) was utilized. We used X-ray photoelectron spectroscopy (XPS; K-alpha, Thermo Scientific, Waltham, MA, USA) for the chemical analysis of the materials. The contour of the sensor device with $Co(OH)_xF_{2-x}$ powders was scanned by a 3D profiler (Contour GT-X, Bruker, Billerica, MA, USA). The Brunauer–Emmett–Teller (BET; Micromeritics, Norcross, GA, USA) surface area of the $Co(OH)_xF_{2-x}$ nanosheets was determined from nitrogen adsorption-desorption isotherm. The SEM equipment used in this study is located at the MEMS·Sensor Platform Center of SungKyunKwan University (SKKU), Suwon, Korea.

2.3. Fabrication of Gas Sensor and Gas-Sensing Measurements

The detailed fabrication process of interdigitated (IDT) electrodes and details of gas-sensing system are reported in our previous work [23]. $Co(OH)_xF_{2-x}$ nanosheet powders were dissolved in DI water (0.5 wt. %) and drop-coated on the IDT electrodes on a hot plate (100 °C). After full evaporation of the solvent, these devices were used for gas-sensing measurements (see Figure S2). Besides, some of the sensors were annealed at 300, 350, 400, and 450 °C for 2 or 4 h to investigate the effects of post-annealing conditions on the materials. For additional platinum (Pt) doping on the materials, a 1 nm-thick Pt film was loaded on the $Co(OH)_xF_{2-x}$ nanosheets of the devices using a magnetron sputtering system. A home-made gas-sensing system was described in our previous study. Gas-sensing characteristics were investigated for acetone (CH_3COCH_3), toluene ($C_6H_5CH_3$), carbon monoxide (CO), hydrogen (H_2), and nitrogen dioxide (NO_2), which were diluted with dry air (2 L/min) using mass flow controllers (MFCs). The relative humidity (RH) of the laboratory varied from 30 to 63% and that of the sensing chamber was kept at 10% for all sensing tests. The operating temperature of gas sensors was controlled from 25 to 350 °C by Joule heating using a ceramic heater connected to a power supplier. The response of the test is defined as $[(R_g - R_a)/R_a]*100$ or $[(R_a - R_g)/R_g]*100$ for

reactions with reducing gases and oxidizing gases, respectively, where R_a and R_g represent resistances in ambient and an analyte gas.

3. Results

3.1. Synthesis and Characterization of $Co(OH)_xF_{2-x}$ Nanosheets

The morphology of the templates of SiO_2 spheres and the material hydrothermally grown on the templates were characterized using SEM, as shown in Figure 2. Figure 2a,b indicates that the SiO_2 spheres were fabricated with a good dispersity, clean surface, and uniform size. The average diameter of the SiO_2 spheres is around 160 nm. Figure 2c,d shows the morphology of the material grown on the templates after removal of the templates. It consists of very thin, very curly sheets, which appear clustered around what seem to have been occupied by the SiO_2 spheres before the removal.

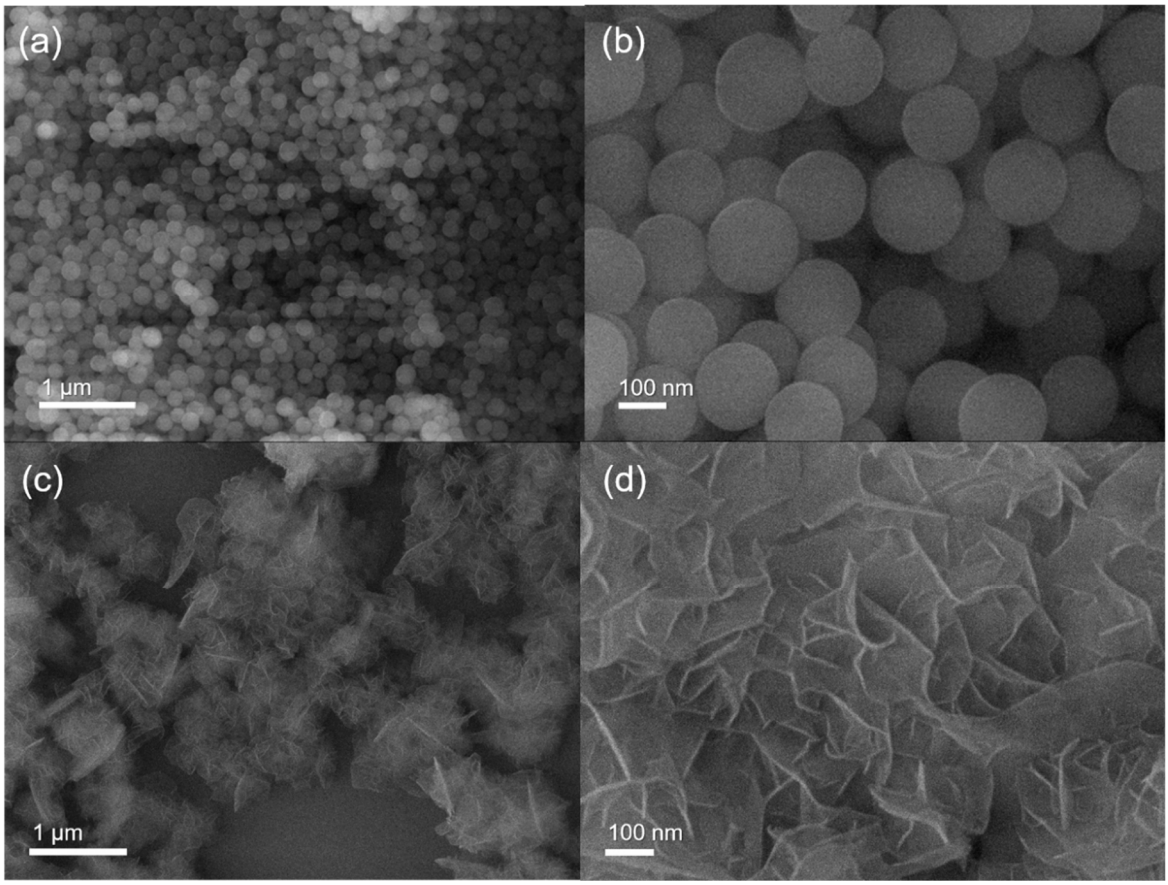

Figure 2. SEM images of (**a**,**b**) SiO_2 spheres and (**c**,**d**) $Co(OH)_xF_{2-x}$ nanosheets.

We employed XPS to investigate the chemical state of the synthesized material. Figure 3a–c present XPS analysis results on the peaks of F 1s, Co 2p, and O 1s. The binding energy of the F 1s (~684.3 eV) peak is close with that reported in a previous study on Co(OH)F [9]. Co 2p subpeaks corresponding to inorganic Co^{2+} species with unpaired 3d electrons and mainly appear at 781.1 ± 0.05 and 783.3 ± 0.05 (Co $2p_{1/2}$), and 796.9 ± 0.05 and 798.0 ± 0.05 eV (Co $2p_{3/2}$), which are somewhat higher than the binding energies of Co^{3+} species [17,18,24]. Other subpeaks at 785.9 ± 0.05, and 803.2 ± 0.05 eV are ascribed to the Co^{2+} shake-up satellite [18]. The O 1s peak is deconvoluted into two subpeaks—a large one at 531.6 ± 0.05 eV corresponding to metal hydroxides and a small one at 533.5 ± 0.05 eV from organic contaminants [9]. A quantitative analysis of the XPS data discloses that the fluorine content in the sample is substantial (peak intensity ratio between F and Co peaks (F/Co): ~25%), much higher than that obtained via doping (F/Co: ~10%) [15]. Figure 3d shows an XRD pattern of the

synthesized material, which exhibits very small peaks at positions close to those of the orthorhombic Co(OH)F phase. It is interesting to note the asymmetric bundle of peaks at 32~45°, an unusual feature reported also in other studies on $Co(OH)_2$ materials [25,26]. These data of XRD and XPS suggest that the synthesized material could be amorphous or nanocrystalline $Co(OH)_xF_{2-x}$ with a broad range of fluorine compositions.

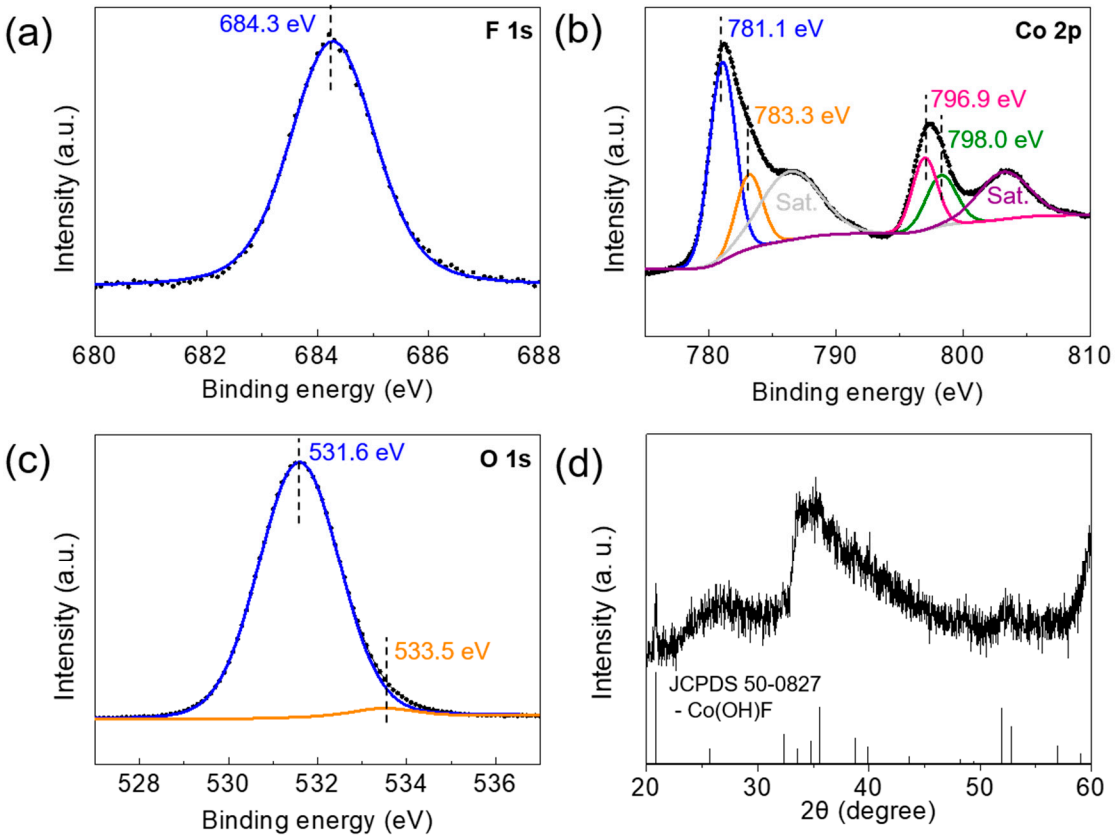

Figure 3. X-ray photoelectron spectroscopy (XPS) spectra of the $Co(OH)_xF_{2-x}$ nanosheets ((**a**) F 1s, (**b**) Co 2p, and (**c**) O 1s), and X-ray diffraction (XRD) pattern of the $Co(OH)_xF_{2-x}$ nanosheets (**d**).

In the TEM images shown in Figure 4a,b, the sheets appear highly electron-transparent, confirming that they are very thin, probably only a few atomic layers thick. The morphology of the nanosheets suggests that they have been densely grown around SiO_2 spheres, the places of which now appear empty because of the removal of the spheres via aging (for example, see the box in Figure 4a). The BET analysis confirmed that the specific surface area of the material was around 193.38 m^2 g^{-1}, a value larger than or comparable with those of 2D materials such as graphene and MoS_2 (see Figure S3 for the BET data) [27–29].

Figure 4c shows elemental mapping acquired from the EDS analysis for the area shown in Figure 4b, exhibiting that Co, O, and F are uniformly distributed throughout the sheets. Figure 4d,e shows high-resolution TEM (HRTEM) images of the $Co(OH)_xF_{2-x}$ nanosheets, showing that the material is mainly amorphous, without any noticeable long-range order. Nevertheless, a close look into the image discloses that there are many areas (some marked with yellow circles) showing some short-range ordering. Analysis on such short-range ordering areas indicates that the plane spacings are close to those of Co(OH)F, as shown in Figure 4e [19]. These results confirm that the synthesized nanosheets are amorphous $Co(OH)_xF_{2-x}$ with some short-range ordering. In addition, it should be also noted from the EDS analysis that although the SiO_2 spheres were supposedly removed as a whole through the removal process, the analysis indicates that there are some Si atoms uniformly distributed over the

$Co(OH)_xF_{2-x}$ nanosheets, implying that the removal process did not fully remove SiO_2 but rather left some redistributed over the nanosheets.

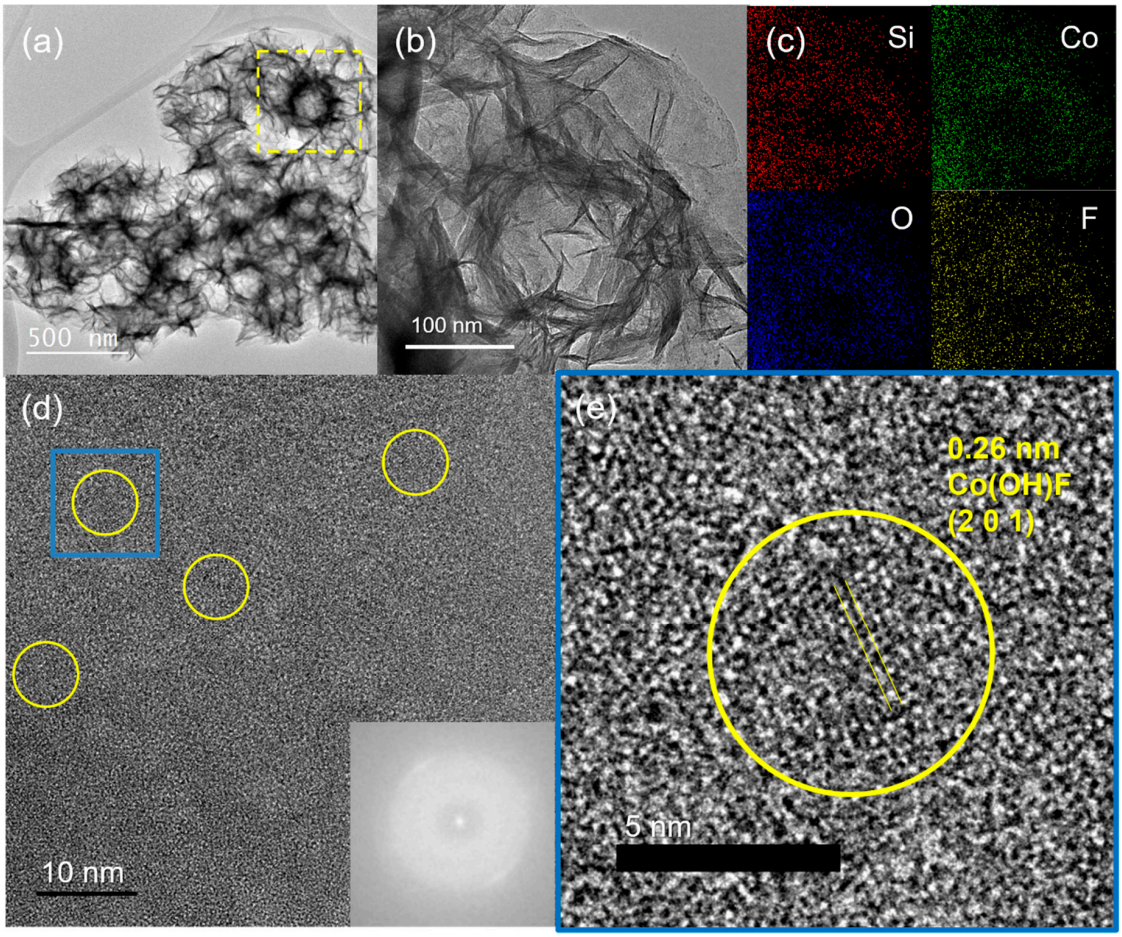

Figure 4. Transmission Electron Microscopy (TEM) analysis of the $Co(OH)_xF_{2-x}$ nanosheets: (**a**,**b**) bright-field images, (**c**) electron dispersive spectroscopy (EDS) mapping, and (**d**,**e**) high-resolution images. An inset image in (d) is a FFT (Fast Fourier Transform) pattern of the high-resolution image.

3.2. Post-Annealing Effects on $Co(OH)_xF_{2-x}$ Nanosheets

For sensor applications, it is important to ensure the thermal stability of sensing materials since sensors are usually operated at elevated temperatures. Figure 5 exhibits SEM images of $Co(OH)_xF_{2-x}$ nanosheets on a sensor device annealed at 350 °C for 2 h, showing that the nanosheet cluster structure remains stable. Figure 6a shows the fluorine content (F/Co*100) acquired from an XPS analysis for the samples of $Co(OH)_xF_{2-x}$ nanosheets synthesized with SiO_2 templates and without templates after annealing at various temperatures for 2 h. It is clear that the F ratio in the nanosheets decreases with the post-annealing temperature increasing, suggesting that F evaporates at high temperatures. It should be also noted that the sample grown on the template has retained fluorine more effectively at elevated temperatures than the sample without a template, implying that the SiO_2 template has possibly played some role in retaining F.

Our FTIR analysis sheds some light on the possible influence of the SiO_2 template on retaining fluorine, as shown in Figure 6b. In the FTIR data, the sample synthesized with SiO_2 shows a strong peak at 1020 cm^{-1}, corresponding to bonding between Si and F, which does not decline upon annealing at elevated temperatures [30]. In contrast, the no-template sample does not show any peak at 1020 cm^{-1} but a large one at 650 cm^{-1}, which could be attributed to Co–O bonding [31]. These data indicate that

the remnants of the SiO_2 templates have possibly helped hold fluorine atoms (prone to evaporation) effectively by providing a strong bond with Si.

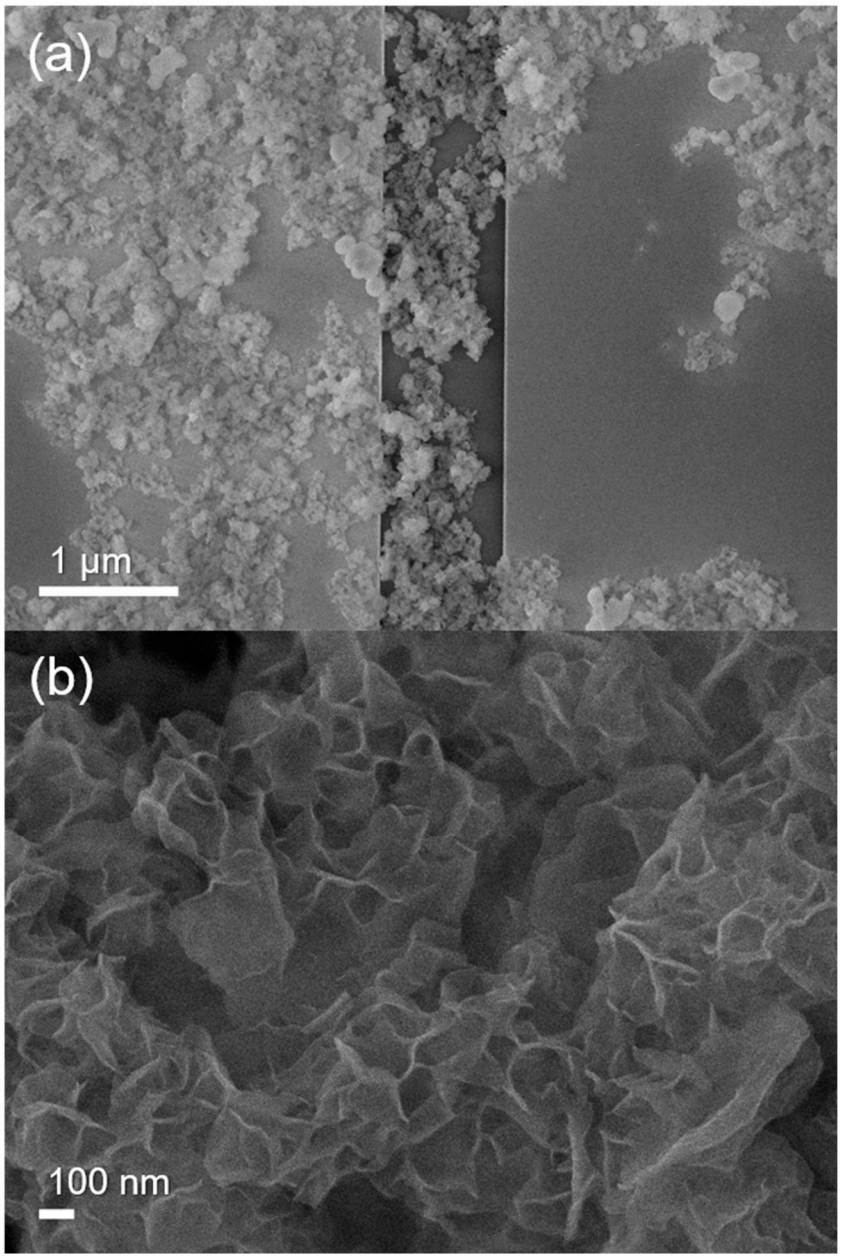

Figure 5. (**a**) High- and (**b**) low-resolution SEM images of the $Co(OH)_xF_{2-x}$ nanosheets annealed at 350 °C for 2 h on device.

The TEM investigation further indicated no difference in the morphology of nanosheets before and after post-annealing at 350, 400, and 450 °C (see Figure S4). Figure 7 displays the high-resolution TEM images of the $Co(OH)_xF_{2-x}$ nanosheets annealed at 350, 400, and 450 °C. A careful observation of the images of Figure 7a,d, and g reveals that the nanosheets have become nanocrystalline. Some of the nanocrystals are Co(OH)F while others belong to Co_3O_4 according to d-spacing analysis (see the images of the center and right-side columns). These results indicate that a significant part of the material has been transformed into Co_3O_4 upon post-annealing.

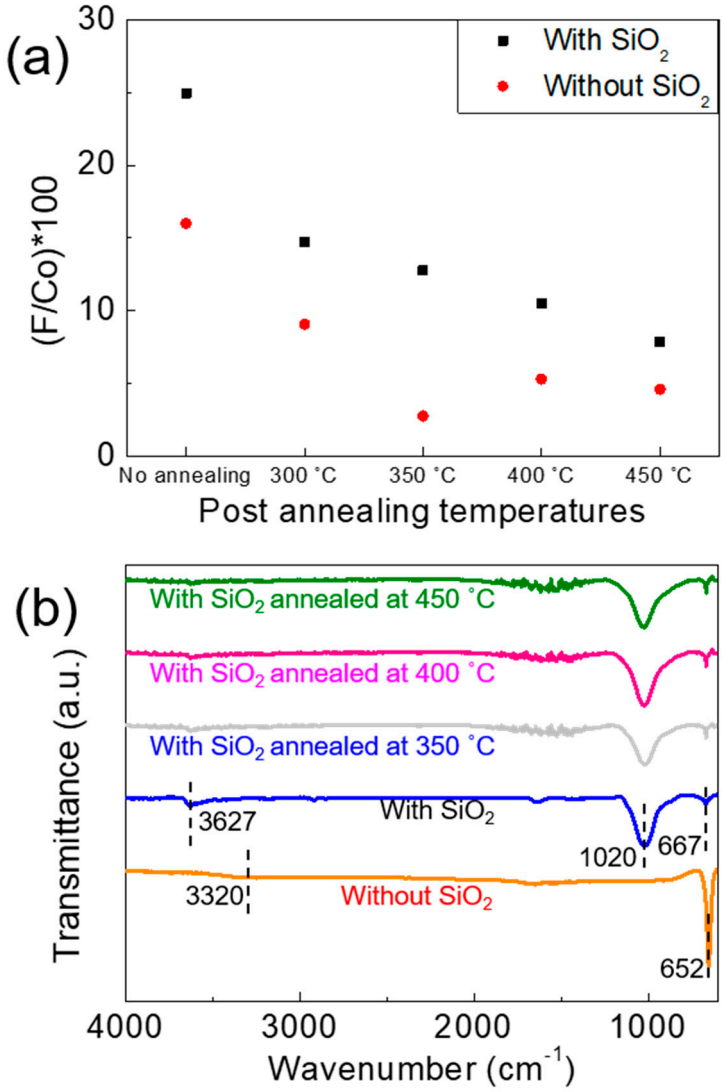

Figure 6. (**a**) Annealing temperature effects on the contents of fluorine (F/Co*100), acquired from XPS, in the nanosheets synthesized with and without SiO_2 template, and (**b**) comparison of the Fourier transform infrared spectroscopy (FTIR) spectra of the samples.

3.3. Gas-Sensing Characteristics of $Co(OH)_xF_{2-x}$ Nanosheet Sensors

We evaluated the gas-sensing ability of the sensor based on the $Co(OH)_xF_{2-x}$ nanosheets by examining the operating temperature, acetone gas concentration, gas species, and time elapse effects. Figure 8a shows gas responses at operating temperatures of 25, 43, 72, 150, 200, and 250 °C. The response graph exhibits a typical volcano shape with an optimized operating temperature of 200 °C. The response at 200 °C is around 269% toward acetone gas at a concentration of 4.5 ppm. For such a low acetone concentration, a response of 269% is quite high, compared with those of other reports on various cobalt-based materials for acetone gas sensor applications, as shown in Table 1.

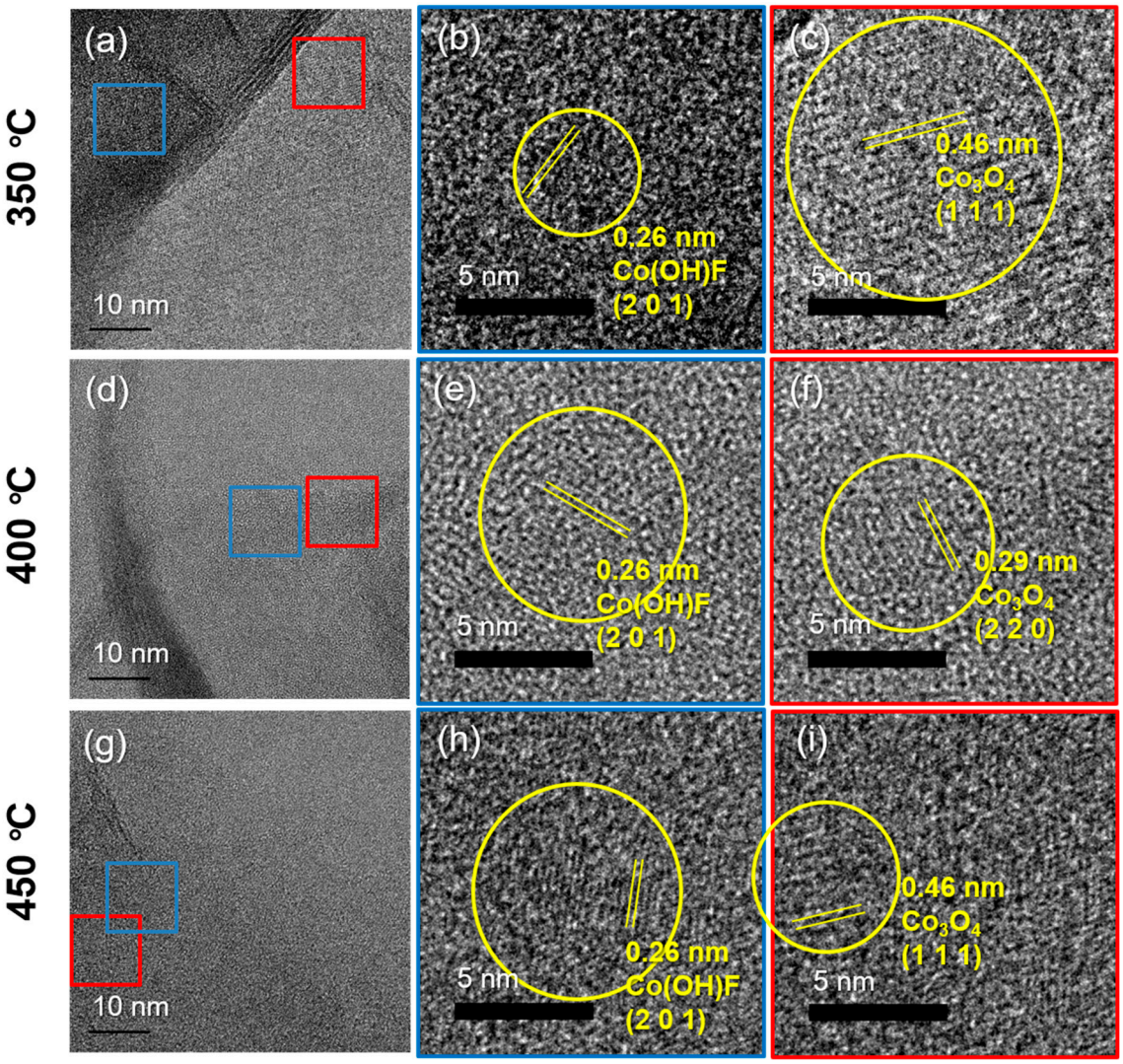

Figure 7. High-resolution TEM images of the $Co(OH)_xF_{2-x}$ nanosheets annealed at (**a**–**c**) 350, (**d**–**f**) 400, and (**g**–**j**) 450 °C for 2 h. (**b**,**e**,**h**) and (**c**,**f**,**i**) are the magnified images of the blue and red squares in (**a**,**d**,**g**), respectively.

Figure 8b shows dynamic sensing characteristics of the sensor upon the input of acetone gas at various concentrations at 200 °C. Calculated responses at each acetone concentration were also plotted (see Figure S5). The limit of detection of the sensor toward acetone gas is 0.04 ppm with a response of 17%. The sensor also shows a good selectivity toward other gases such as CH_3COCH_3 (2.2 ppm), $C_6H_5CH_3$ (3.6 ppm), CO (0.8 ppm), H_2 (0.8 ppm), and NO_2 (1.1 ppm) at 200 °C, as shown in Figure 8c. Figure 8d shows responses to 4.5-ppm acetone gas as a function of time elapse for 20 days. The response of the $Co(OH)_xF_{2-x}$ nanosheet-based sensor degrades from 269 at the first measurement to 106% after 6 days and stayed at a similar level during following measurements.

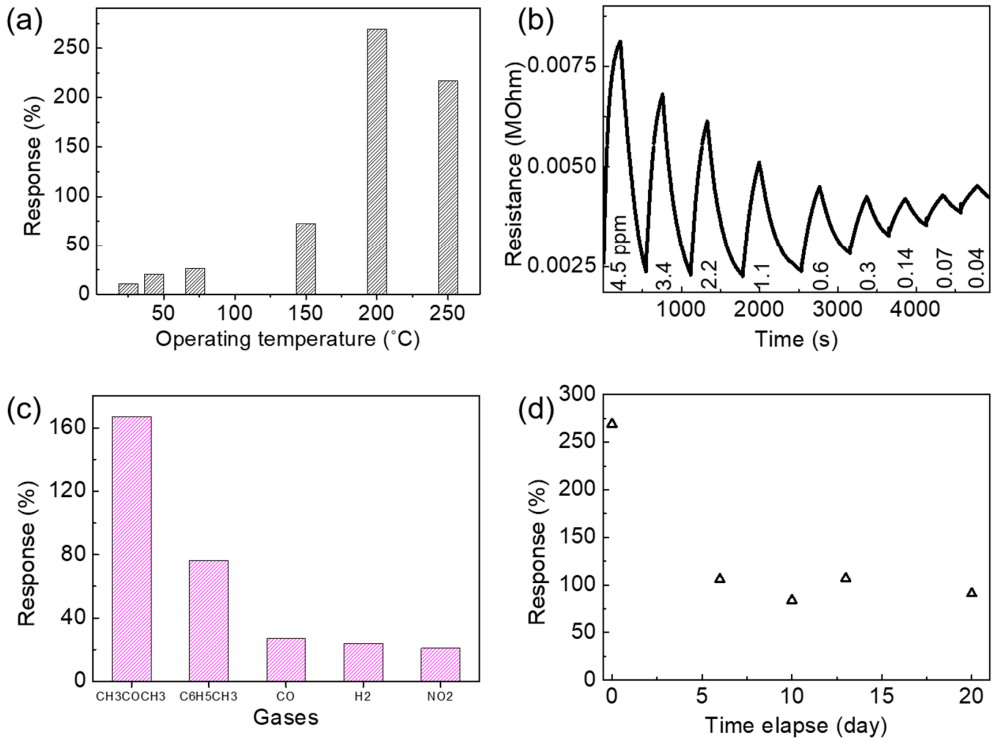

Figure 8. Sensing characteristics of a sensor based on $Co(OH)_xF_{2-x}$ nanosheets: (**a**) responses at various operating temperatures toward 4.5 ppm of acetone gas, (**b**) resistance changes upon input of acetone gas of a various concentration at 200 °C, (**c**) selectivity toward CH_3COCH_3 (2.2 ppm), $C_6H_5CH_3$ (3.6 ppm), CO (0.8 ppm), H_2 (0.8 ppm), and NO_2 (1.1 ppm) at 200 °C, and (**d**) stability (for 20 days) toward 4.5 ppm of acetone at 200 °C.

Table 1. Comparison of the performances of acetone sensors using Co-based materials reported in the literature.

Material	Operating Temp. (°C)	Concentration (ppm)	Response (R_g/R_a)	Reference
Hierarchical and hexagonal Co_3O_4	240	2	1.32	[32]
Co_3O_4 crossed nanosheet arrays	111	20	6.8	[1]
Meso- and macroporous Co_3O_4 nanorods	300	74,570	18.5	[33]
Rhombus-shaped Co_3O_4 nanorod arrays	160	500	20.1	[20]
Co_3O_4 core-shell	190	200	13	[34]
Bamboo raft-like Co_3O_4	180	200	10.5	[35]
Ultrathin porous Co_3O_4 nanosheets	150	100	11.4	[36]
Co_3O_4 nanosheets	160	100	6.1	[37]
Ce-doped $CoFe_2O_4$	225	5000	1.77	[38]
Hollow ZnO/Co_3O_4	300	1	1.5	[39]
Multi-shelled $ZnCo_2O_4$	200	0.5	1.36	[40]
PdO Catalyst functionalized Co_3O_4 hollow nanocages	350	5	2.51	[7]
ZnO/$ZnCo_2O_4$ nanotubes	175	50	15	[41]
Co_3O_4/$ZnCo_2O_4$	255	100	16.3	[42]
$Co(OH)_xF_{2-x}$ nanosheets	200	4.5	3.69 (269%)	Our study
		1.1	2.17 (117%)	
		0.04	1.17 (17%)	
Pt-doped $Co(OH)_xF_{2-x}$ nanosheets-annealed at 300 °C	300	4.5	1.77 (77%)	

3.4. Gas-Sensing Characteristics of Annealed $Co(OH)_xF_{2-x}$ Nanosheet Sensors and Pt-Doping Effect

Next, we examined if the sensor functioned effectively at high temperatures (≤450 °C). We investigated dynamic sensing characteristics by changing the operating temperature between 200 and 300 °C toward acetone gas (4.5 ppm), as shown in Figure 9a,b. In the first cycle, the sensor

shows a stable response and recovery at 200 °C, whereas it displays an unstable behavior at 250 and 300 °C [14]. We also noticed some color change of the material (from pink to dark brown) on the device during measurements at elevated temperatures (see the photographs in Figure 9a), an indication of the deterioration of the material, possibly due to fluorine evaporation [20].

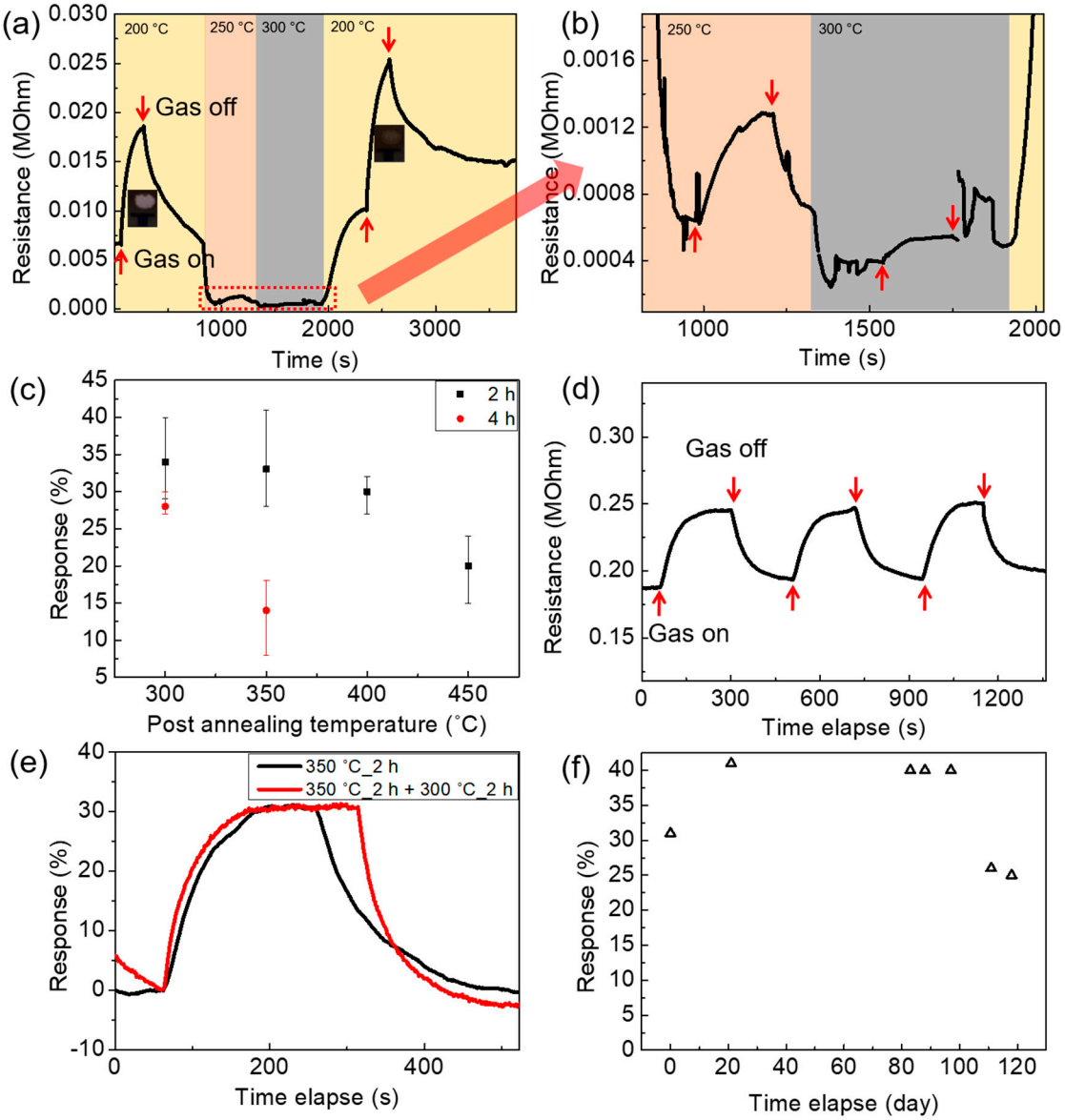

Figure 9. (**a**,**b**) Dynamic sensing characteristics upon changes of applied temperature toward 4.5 ppm of acetone gas. (**c**) Responses of annealed $Co(OH)_xF_{2-x}$ nanosheet sensors with various post-annealing conditions. Dynamic sensing characteristics of the sample after post-annealing at 350 °C for 2 h (**d**) and after additional annealing at 300 °C for 2 h (**e**). (**f**) Long-term stability test of the 350 °C sample for 118 days toward 4.5 ppm of acetone gas at 300 °C.

We tested the sensors after post-annealing at 300 to 450 °C to further investigate the temperature effects on sensor performance. Figure 9c displays the gas responses of sensors annealed at 300, 350, 400, and 450 °C for 2 or 4 h toward 4.5 ppm acetone at 300 °C, which show much lower responses than those measured before post-annealing. It should be noted that the trend of the response, decreasing with the post-annealing temperature increasing, is similar to that of the fluorine concentration with temperature (see Figure 6a), hinting that the loss of fluorine possibly influenced the response to acetone

gas. Increasing the post-annealing time from 2 to 4 h also deteriorates the gas response to 28 and 14% at 300 and 350 °C, respectively, as shown in Figure 9c.

Using the sample annealed at 350 °C for 2 h, we further performed a dynamic test, finding that although the response is low, the sensor works reliably with a full recovery for three successive gas on/off cycles at 300 °C, as shown in Figure 9d. Furthermore, additional annealing at 300 °C for 2 h does not decrease the response, as shown in Figure 9e, suggesting that once the sensing material is annealed at 350 °C, further annealing at a lower temperature would not affect the response much. The result of a long-term stability test shown in Figure 9d also exhibits stable operations with a similar response level for around 3 months. Thus, the annealed sensor at 350 °C shows stable responses although the response level is significantly lower, as compared to the performance of the non-annealed sensor.

It is well known that noble metal dopants such as Pt, Pd, and Au could enhance gas sensor responses because of their strong catalytic properties [43]. In an effort to recover the deteriorated gas response of the 350 °C sample, we loaded Pt (1 nm) on the sensor and conducted measurements for performance (Figure 10). Figure 10a clearly shows improvements in responses at all working temperatures after loading Pt to the device. The sensor also demonstrated a good selectivity toward 4.5 ppm of acetone gas, compared to 4.5 ppm of other gases such as $C_6H_5CH_3$, CO, H_2, and NO_2, as shown in Figure 10b. Figure 10c presents a good sensitivity of the sensor toward acetone at a concentration of 1.1, 2.2, 3.4, and 4.5 ppm. Dynamic sensing characteristics in Figure 10d displays responses of stepwise increase upon the injection of acetone with the concentration increasing from 1.1 to 4.5 ppm, showing a sensitive response at each step and full recovery upon stopping the injection of acetone gas. These data confirm that the Pt loading on the sensor device has enhanced the sensing response, enabling a sensor with a high sensitivity and good stability.

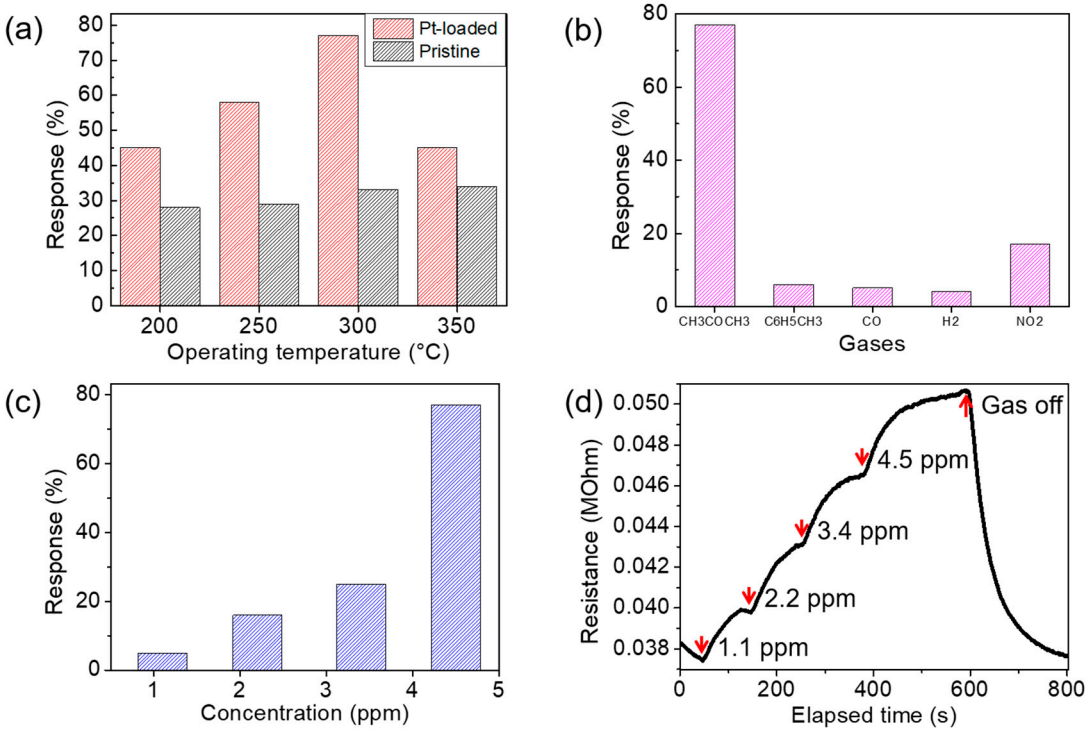

Figure 10. Sensing characteristics of Pt-doped $Co(OH)_xF_{2-x}$ nanosheet sensors annealed at 350 °C for 2 h. Responses at various operating temperatures compared with a pristine sample toward 4.5 ppm of acetone gas (**a**), toward various gases of 4.5 ppm (CH_3COCH_3, $C_6H_5CH_3$, CO, H_2, and NO_2) at 300 °C (**b**), and toward various acetone concentrations at 300 °C (**c**). (**d**) Dynamic sensing characteristics of the sensor toward an increasing acetone gas concentration at 350 °C.

3.5. Gas-Sensing Mechanisms

In this study, we synthesized $Co(OH)_xF_{2-x}$ nanosheets, a material successfully incorporating a high concentration of fluorine and keeping it to some extent through annealing at elevated temperatures (owing to the support from the bond with Si of the remnant SiO_2). It is clear from our sensor data that the presence of fluorine of a high concentration helped achieve a high gas response. In comparison, a sensor based on a material fabricated without adding NH_4F in the synthesis process showed a low response (92%) (see Figure S6), highlighting the effects of F.

It should be noted that incorporated F, with a high electronegativity, could enhance the Lewis acidity of the material, which could facilitate the adsorption of gas molecules [15,16,19]. For the present study, the main reactions occurring at the surface of the $Co(OH)_xF_{2-x}$ nanosheets can be expressed as shown below [1,44,45]. The high Lewis acidity of the nanosheets with a high concentration of F has possibly helped the material accept electrons easily and promoted the reaction of Equation (4).

$$O_2(gas) \rightarrow O_2(ads) \quad (1)$$

$$O_2(ads) + e^- \rightarrow O_2{}^-(ads)\ (T < 100\ ^\circ C) \quad (2)$$

$$O_2{}^-(ads) + e^- \rightarrow 2O^-(ads)\ (100\ ^\circ C < T < 300\ ^\circ C) \quad (3)$$

$$CH_3COCH_3(gas) + 8O^-(ads) \rightarrow 3CO_2 + 3H_2O + 8e^- \quad (4)$$

$$e^- + h^+ \rightarrow Null \quad (5)$$

In addition, the morphology of the $Co(OH)_xF_{2-x}$ nanosheets with a high specific surface area (193.38 m^2/g), brought about by the assistance of the SiO_2 template, has possibly contributed to the high sensing performance. For example, the high response of the $Co(OH)_xF_{2-x}$ nanosheets (269%) toward 4.5 ppm of acetone gas at 200 °C contrasts with the low response (147%) of the sensor based on $Co(OH)_xF_{2-x}$ fabricated without SiO_2 templates, which has a bulk-type morphology (see Figure S7). Other studies also show the strong influence of morphology on the sensitivity of sensors, attributing to the increase in oxygen-adsorption sites promoting the reaction of Equation (1) [46,47]. Thus, the adoption of an SiO_2 template in the synthesis process played a beneficial role in two ways, maintaining a high F concentration for a high catalytic property and producing a structure with a very high specific surface area.

4. Conclusions

We synthesized $Co(OH)_xF_{2-x}$ nanosheets by adopting SiO_2 sphere templates and fabricated sensor devices based on the materials. Our material characterization using such analytical tools as XPS, FTIR, and TEM confirms that the material is made up of $Co(OH)_xF_{2-x}$ nanosheets containing a high concentration of F with an amorphous microstructure with some short-range ordering. The sensor based on the $Co(OH)_xF_{2-x}$ nanosheets exhibited a very high response of 269% toward 4.5 ppm of acetone gas at an operation temperature of 200 °C, and a minimum detection limit of 40 ppb was obtained. Although the sensor showed some indications of degradation (possibly due to F evaporation) at a temperature higher than 300 °C, the Pt doping was found to help recover gas response to some extent (77% toward 4.5 ppm of acetone). We discussed the strong catalytic property of F in a high concentration as well as the high specific surface area due to the morphology of densely clustered nanosheets being responsible for the excellent sensor performance. This study highlights the possibility of further applications of a new material group of metal fluoride hydroxides to gas sensors owing to their distinct advantages compared to conventional metal oxide materials.

Supplementary Materials: The Supplementary Materials are available online at http://www.mdpi.com/2073-4352/10/11/968/s1. Figure S1. EDS spectrum of $Co(OH)_xF_{2-x}$ nanosheets with atomic percentages of each element. Figure S2. Profile image of the interdigitated sensor device with coated $Co(OH)_xF_{2-x}$ nanosheets powders. Figure S3. N2 adsorption-desorption isotherm with calculated BET surface area (193.38 m2/g). Figure S4. TEM

bright-field images of the $Co(OH)_xF_{2-x}$ nanosheets (a) before and after annealing at (b) 350, (c) 400, and (d) 450 °C for 2 h. Figure S5. Responses of $Co(OH)_xF_{2-x}$ nanosheets-based sensor toward acetone gas of various concentrations at 200 °C. Figure S6. Responses of a material synthesized without NH_4F (other synthesis procedures were same with the $Co(OH)_xF_{2-x}$ nanosheets) at various temperatures toward 4.5 ppm of acetone (Responses of this material at temperatures lower than 150 °C were immeasurable because of high resistance). Figure S7. Responses of $Co(OH)_xF_{2-x}$ without SiO2 templates at various temperatures toward 4.5 ppm of acetone.

Author Contributions: Conceptualization, Y.Y. and T.-y.E.; methodology, Y.Y. and T.-y.E.; software, S.X. and P.J.Y.; validation, J.-S.P. and H.-J.L.; formal analysis, T.-y.E.; investigation, T.-y.E.; resources, J.-S.P. and H.-J.L.; data curation, T.-y.E., J.-S.P. and H.-J.L.; writing—original draft preparation, T.-y.E.; writing—review and editing, Y.Y., C.Y., J.-S.P. and H.-J.L.; visualization, S.X. and P.J.Y.; supervision, J.-S.P. and H.-J.L.; project administration, J.-S.P. and H.-J.L.; funding acquisition, J.-S.P. and H.-J.L. All authors have read and agreed to the published version of the manuscript.

Funding: This work was supported by the Korea Basic Science Institute (KBSI) National Research Facilities and Equipment Center (NFEC) grant funded by the Korea government (Ministry of Education) (No. 2019R1A6C1030010). This work was also financially supported by National Natural Science Foundation of China (NSFC, 61904190). Additionally, J.-S. Park was partially supported by Project No. P0006858 of International Collaboration Program by KIAT and MOTIE in Rep. Korea.

Conflicts of Interest: The authors declare no conflict of interest.

References

1. Zhang, Z.; Zhu, L.; Wen, Z.; Ye, Z. Controllable synthesis of Co_3O_4 crossed nanosheet arrays toward an acetone gas sensor. *Sens. Actuators B Chem.* **2017**, *238*, 1052–1059. [CrossRef]
2. Kao, K.-W.; Hsu, M.-C.; Chang, Y.-H.; Gwo, S.; Yeh, J.A. A sub-ppm acetone gas sensor for diabetes detection using 10 nm thick ultrathin InN FETs. *Sensors* **2012**, *12*, 7157–7168. [CrossRef]
3. Xie, Y.; Xing, R.; Li, Q.; Xu, L.; Song, H. Three-dimensional ordered ZnO–CuO inverse opals toward low concentration acetone detection for exhaled breath sensing. *Sens. Actuators B Chem.* **2015**, *211*, 255–262. [CrossRef]
4. Barsan, N.; Koziej, D.; Weimar, U. Metal oxide-based gas sensor research: How to? *Sens. Actuators B Chem.* **2007**, *121*, 18–35. [CrossRef]
5. Zeng, Y.; Zhang, T.; Yuan, M.; Kang, M.; Lu, G.; Wang, R.; Fan, H.; He, Y.; Yang, H. Growth and selective acetone detection based on ZnO nanorod arrays. *Sens. Actuators B Chem.* **2009**, *143*, 93–98. [CrossRef]
6. Kou, X.; Xie, N.; Chen, F.; Wang, T.; Guo, L.; Wang, C.; Wang, Q.; Ma, J.; Sun, Y.; Zhang, H. Superior acetone gas sensor based on electrospun SnO_2 nanofibers by Rh doping. *Sens. Actuators B Chem.* **2018**, *256*, 861–869. [CrossRef]
7. Koo, W.-T.; Yu, S.; Choi, S.-J.; Jang, J.-S.; Cheong, J.Y.; Kim, I.-D. Nanoscale PdO catalyst functionalized Co_3O_4 hollow nanocages using MOF templates for selective detection of acetone molecules in exhaled breath. *ACS Appl. Mater. Interfaces* **2017**, *9*, 8201–8210. [CrossRef]
8. Li, W.-Y.; Xu, L.-N.; Chen, J. Co_3O_4 nanomaterials in lithium-ion batteries and gas sensors. *Adv. Funct. Mater.* **2005**, *15*, 851–857. [CrossRef]
9. Wan, S.; Qi, J.; Zhang, W.; Wang, W.; Zhang, S.; Liu, K.; Zheng, H.; Sun, J.; Wang, S.; Cao, R. Hierarchical Co(OH)F Superstructure Built by Low-Dimensional Substructures for Electrocatalytic Water Oxidation. *Adv. Mater.* **2017**, *29*, 1700286. [CrossRef]
10. Zhou, T.; Zhang, T.; Deng, J.; Zhang, R.; Lou, Z.; Wang, L. P-type Co_3O_4 nanomaterials-based gas sensor: Preparation and acetone sensing performance. *Sens. Actuators B Chem.* **2017**, *242*, 369–377. [CrossRef]
11. Kang, J.-S.; Park, J.-S.; An, B.-S.; Yang, C.-W.; Lee, H.-J. Nickel Doping on Cobalt Oxide Thin Film Using by Sputtering Process-a Route for Surface Modification for p-type Metal Oxide Gas Sensors. *J. Korean Phys. Soc.* **2018**, *73*, 1867–1872. [CrossRef]
12. Vladimirova, S.; Krivetskiy, V.; Rumyantseva, M.; Gaskov, A.; Mordvinova, N.; Lebedev, O.; Martyshov, M.; Forsh, P. Co_3O_4 as p-type material for CO sensing in humid air. *Sensors* **2017**, *17*, 2216. [CrossRef] [PubMed]
13. Zhang, C.; Li, L.; Hou, L.; Chen, W. Fabrication of Co_3O_4 nanowires assembled on the surface of hollow carbon spheres for acetone gas sensing. *Sens. Actuators B Chem.* **2019**, *291*, 130–140. [CrossRef]
14. Xu, K.; Zhao, W.; Yu, X.; Duan, S.; Zeng, W. MOF-derived Co_3O_4/Fe_2O_3 pn hollow cubes for improved acetone sensing characteristics. *Phys. E Low Dimens. Syst. Nanostruct.* **2020**, *118*, 113869. [CrossRef]

15. Barreca, D.; Bekermann, D.; Comini, E.; Devi, A.; Fischer, R.A.; Gasparotto, A.; Gavagnin, M.; Maccato, C.; Sada, C.; Sberveglieri, G. Plasma enhanced-CVD of undoped and fluorine-doped Co_3O_4 nanosystems for novel gas sensors. *Sens. Actuators B Chem.* **2011**, *160*, 79–86. [CrossRef]
16. Zhao, Y.; Du, X.; Wang, X.; He, J.; Yu, Y.; He, H. Effects of F doping on TiO_2 acidic sites and their application in QCM based gas sensors. *Sens. Actuators B Chem.* **2010**, *151*, 205–211. [CrossRef]
17. Song, M.; Zhang, Z.; Li, Q.; Jin, W.; Wu, Z.; Fu, G.; Liu, X. Ni-foam supported Co(OH)F and Co–P nanoarrays for energy-efficient hydrogen production via urea electrolysis. *J. Mater. Chem. A* **2019**, *7*, 3697–3703. [CrossRef]
18. Wang, Z.; Liu, Z.; Du, G.; Asiri, A.M.; Wang, L.; Li, X.; Wang, H.; Sun, X.; Chen, L.; Zhang, Q. Ultrafine PtO_2 nanoparticles coupled with a Co(OH)F nanowire array for enhanced hydrogen evolution. *Chem. Commun.* **2018**, *54*, 810–813. [CrossRef] [PubMed]
19. Lv, J.; Yang, X.; Zang, H.-Y.; Wang, Y.-H.; Li, Y.-G. Ultralong needle-like N-doped Co(OH)F on carbon fiber paper with abundant oxygen vacancies as an efficient oxygen evolution reaction catalyst. *Mater. Chem. Front.* **2018**, *2*, 2045–2053. [CrossRef]
20. Wen, Z.; Zhu, L.; Mei, W.; Hu, L.; Li, Y.; Sun, L.; Cai, H.; Ye, Z. Rhombus-shaped Co_3O_4 nanorod arrays for high-performance gas sensor. *Sens. Actuators B Chem.* **2013**, *186*, 172–179. [CrossRef]
21. Wang, W.; Gu, B.; Liang, L.; Hamilton, W.A. Fabrication of near-infrared photonic crystals using highly-monodispersed submicrometer SiO_2 spheres. *J. Phys. Chem. B* **2003**, *107*, 12113–12117. [CrossRef]
22. Simmonov, Y.A.; Kritskii, A.A.; Rychkov, V.N.; Tomashov, V.A. Investigation of the treatment process of associated dioxides of zirconium and silicon by an aqueous solution of ammonium fluoride. *Rus. J. Non Ferr. Met.* **2010**, *51*, 320–323. [CrossRef]
23. Nundy, S.; Eom, T.-Y.; Song, K.-Y.; Park, J.-S.; Lee, H.-J. Hydrothermal synthesis of mesoporous ZnO microspheres as NO_X gas sensor materials—Calcination effects on microstructure and sensing performance. *Ceram. Int.* **2020**, *46*, 19354–19364. [CrossRef]
24. Yang, J.; Liu, H.; Martens, W.N.; Frost, R.L. Synthesis and characterization of cobalt hydroxide, cobalt oxyhydroxide, and cobalt oxide nanodiscs. *J. Phys. Chem. C* **2010**, *114*, 111–119. [CrossRef]
25. Kong, L.-B.; Liu, M.-C.; Lang, J.-W.; Liu, M.; Luo, Y.-C.; Kang, L. Porous cobalt hydroxide film electrodeposited on nickel foam with excellent electrochemical capacitive behavior. *J. Solid State Electrochem.* **2011**, *15*, 571–577. [CrossRef]
26. Zhou, W.-J.; Zhang, J.; Xue, T.; Zhao, D.-D.; Li, H.-L. Electrodeposition of ordered mesoporous cobalt hydroxide film from lyotropic liquid crystal media for electrochemical capacitors. *J. Mater. Chem.* **2008**, *18*, 905–910. [CrossRef]
27. Niu, Y.; Wang, R.; Jiao, W.; Ding, G.; Hao, L.; Yang, F.; He, X. MoS_2 graphene fiber based gas sensing devices. *Carbon* **2015**, *95*, 34–41. [CrossRef]
28. Zhang, D.; Liu, A.; Chang, H.; Xia, B. Room-temperature high-performance acetone gas sensor based on hydrothermal synthesized SnO_2-reduced graphene oxide hybrid composite. *RSC Adv.* **2015**, *5*, 3016–3022. [CrossRef]
29. Yang, C.; Xiao, F.; Wang, J.; Su, X. 3D flower-and 2D sheet-like CuO nanostructures: Microwave-assisted synthesis and application in gas sensors. *Sens. Actuators B Chem.* **2015**, *207*, 177–185. [CrossRef]
30. Liptak, R.; Yang, J.; Kramer, N.; Kortshagen, U.; Campbell, S. Environmental photostability of SF_6-etched silicon nanocrystals. *Nanotechnology* **2012**, *23*, 395205. [CrossRef]
31. Adam, F.; Thiam-Seng, C. The Production of Hydrogen by Catalytic Oxidation of Hydrocarbons using a Rice Husk Based Cobalt Phyllosilicate Catalyst. *J. Phys. Sci.* **2013**, *24*, 61.
32. Xu, J.; Zhang, J.; Wang, B.; Liu, F. Shape-regulated synthesis of cobalt oxide and its gas-sensing property. *J. Alloys Compd.* **2015**, *619*, 361–367. [CrossRef]
33. Nguyen, H.; El-Safty, S.A. Meso-and macroporous Co_3O_4 nanorods for effective VOC gas sensors. *J. Phys. Chem. C* **2011**, *115*, 8466–8474. [CrossRef]
34. Zhang, R.; Zhou, T.; Wang, L.; Zhang, T. Metal–organic frameworks-derived hierarchical Co_3O_4 structures as efficient sensing materials for acetone detection. *ACS Appl. Mater. Interfaces* **2018**, *10*, 9765–9773. [CrossRef]
35. Wang, S.; Cao, J.; Cui, W.; Fan, L.; Li, X.; Li, D. Facile synthesis of bamboo raft-like Co_3O_4 with enhanced acetone gas sensing performances. *J. Alloys Compd.* **2018**, *758*, 45–53. [CrossRef]
36. Zhang, Z.; Wen, Z.; Ye, Z.; Zhu, L. Gas sensors based on ultrathin porous Co_3O_4 nanosheets to detect acetone at low temperature. *RSC Adv.* **2015**, *5*, 59976–59982. [CrossRef]

37. Lin, Y.; Ji, H.; Shen, Z.; Jia, Q.; Wang, D. Enhanced acetone sensing properties of Co_3O_4 nanosheets with highly exposed (111) planes. *J. Mater. Sci. Mater. Electron.* **2016**, *27*, 2086–2095. [CrossRef]
38. Khandekar, M.; Tarwal, N.; Mulla, I.; Suryavanshi, S. Nanocrystalline Ce doped $CoFe_2O_4$ as an acetone gas sensor. *Ceram. Int.* **2014**, *40*, 447–452. [CrossRef]
39. Zhang, D.; Yang, Z.; Wu, Z.; Dong, G. Metal-organic frameworks-derived hollow zinc oxide/cobalt oxide nanoheterostructure for highly sensitive acetone sensing. *Sens. Actuators B Chem.* **2019**, *283*, 42–51. [CrossRef]
40. Xiong, Y.; Zhu, Z.; Ding, D.; Lu, W.; Xue, Q. Multi-shelled $ZnCo_2O_4$ yolk-shell spheres for high-performance acetone gas sensor. *Appl. Surf. Sci.* **2018**, *443*, 114–121. [CrossRef]
41. Alali, K.T.; Liu, J.; Liu, Q.; Li, R.; Zhang, H.; Aljebawi, K.; Liu, P.; Wang, J. Enhanced acetone gas sensing response of $ZnO/ZnCo_2O_4$ nanotubes synthesized by single capillary electrospinning technology. *Sens. Actuators B Chem.* **2017**, *252*, 511–522. [CrossRef]
42. Qu, F.; Thomas, T.; Zhang, B.; Zhou, X.; Zhang, S.; Ruan, S.; Yang, M. Self-sacrificing templated formation of $Co_3O_4/ZnCo_2O_4$ composite hollow nanostructures for highly sensitive detecting acetone vapor. *Sens. Actuators B Chem.* **2018**, *273*, 1202–1210. [CrossRef]
43. Wang, Y.-D.; Wu, X.-H.; Su, Q.; Li, Y.-F.; Zhou, Z.-L. Ammonia-sensing characteristics of Pt and SiO_2 doped SnO_2 materials. *Solid State Electron.* **2001**, *45*, 347–350. [CrossRef]
44. Lim, S.K.; Hwang, S.-H.; Kim, S.; Park, H. Preparation of ZnO nanorods by microemulsion synthesis and their application as a CO gas sensor. *Sens. Actuators B Chem.* **2011**, *160*, 94–98. [CrossRef]
45. Ge, Y.; Kan, K.; Yang, Y.; Zhou, L.; Jing, L.; Shen, P.; Li, L.; Shi, K. Highly mesoporous hierarchical nickel and cobalt double hydroxide composite: Fabrication, characterization and ultrafast NO_x gas sensors at room temperature. *J. Mater. Chem. A* **2014**, *2*, 4961–4969. [CrossRef]
46. Gao, T.; Wang, T. Synthesis and properties of multipod-shaped ZnO nanorods for gas-sensor applications. *Appl. Phys. A* **2005**, *80*, 1451–1454. [CrossRef]
47. Bie, L.-J.; Yan, X.-N.; Yin, J.; Duan, Y.-Q.; Yuan, Z.-H. Nanopillar ZnO gas sensor for hydrogen and ethanol. *Sens. Actuators B Chem.* **2007**, *126*, 604–608. [CrossRef]